Spatiotemporal multiphysics metamaterials with continuously adjustable functions

Min Lei [a], Liujun Xu [b,*], Jiping Huang [a,**]

[a] *Department of Physics, State Key Laboratory of Surface Physics, and Key Laboratory of Micro and Nano Photonic Structures (MOE), Fudan University, Shanghai, 200438, China*
[b] *Graduate School of China Academy of Engineering Physics, Beijing, 100193, China*

ARTICLE INFO

ABSTRACT

Emerging multiphysics metamaterials offer an exciting opportunity to regulate complex physical processes. However, their functionality and tunability are limited by two severe constraints. Firstly, multiphysics functionality is fixed once structures and materials are prepared, meaning that only one functionality is available for each physical field. Secondly, continuous tunability is challenging to achieve in multiphysics fields because parameters are hard to change on demand. To overcome these limitations, we propose the concept of spatiotemporal multiphysics metamaterials, which takes into account the temporal dimension. The spatiotemporal feature enables multiple functions for each physical field and their continuous switching. We develop rotatable checkerboard structures with different rotation times, material composition, and geometric shapes that allow for flexible thermal and electric function switching between cloaking, sensing, and concentrating. Real-time thermal and electric functions have been theoretically predicted and confirmed by simulations. These results offer a promising spatiotemporal platform for realizing adaptive and intelligent multiphysics field manipulation.

1. Introduction

The ability to control physical fields in complex scenarios is crucial for a wide range of applications, such as power generation [1], radiative cooling [2], biomedical engineering [3], and energy management [4]. Metamaterials [5,6] provide an excellent platform for manipulating various physical fields, including optics [7], acoustics [8], thermotics [9,10], and fluidics [11,12]. Exciting functions like cloaking, sensing, and concentrating allow for the physical field intensity in the working region to be far smaller, equal, or larger than in the background [9,13–15]. With increasing application demands, metamaterial design is evolving beyond the constraint of "one metamaterial for controlling one physical field," and multiphysics metamaterials show significant potential in achieving "one metamaterial for regulating multiple physical fields." This trend has led to the simultaneous control of electromagnetic and acoustic fields [16,17], conductive and convective or radiative fields [18–21], and thermal and electric fields [22–27]. However, existing multiphysics metamaterials still have severe limitations. On the one hand, conventional schemes only offer fixed functions due to the restriction of static structures and materials. On the other hand,

continuous controllability is challenging to achieve because multiphysics parameters are hard to change simultaneously and on demand. Therefore, it remains a significant challenge for multiphysics metamaterials to achieve multiple functions for each physical field, let alone their continuous switching.

Recently, metamaterial designs incorporating the temporal dimension [28,29] have gained significant attention due to their promising degree of freedom. From a fundamental physics perspective, spatiotemporal modulation contributes to unexpected nonreciprocal phenomena [30–36] and intriguing topological transport [37–39]. Additionally, the spatiotemporal approach has practical applications in adaptive thermal camouflage [40] and real-time digital coding [41,42]. However, these spatiotemporal schemes are currently limited to single physical fields. Extending them to multiphysics fields presents a challenging problem as parameters of different physical fields are highly inconvenient to regulate on demand due to structural and material restrictions.

In this study, we propose the concept of spatiotemporal multiphysics metamaterials, which can simultaneously control thermal and electric fields. The temporal dimension is introduced through a rotatable

---

* Corresponding author.
** Corresponding author.
  E-mail addresses: ljxu@gscaep.ac.cn (L. Xu), jphuang@fudan.edu.cn (J. Huang).

checkerboard structure, which allows for continuous tuning of its geometric configuration over time. This feature provides flexible control of thermal and electric conductivities, enabling the realization of various functions in both fields. Our spatiotemporal multiphysics metamaterials offer the flexibility to switch between three or five function combinations, depending on the number of constituent materials used, as shown in Fig. 1a. These results open up new possibilities for flexible and intelligent multiphysics field control, providing unprecedented opportunities for advanced applications.

2. Results and discussion

2.1. Theoretical prediction

Our objective is to develop a single device that can combine various functions for both thermal and electric fields, while allowing for continuous adjustment. One such combination is thermal cloaking plus electric concentrating, which can be achieved through the use of spatiotemporal multiphysics metamaterials composed of rotatable checkerboard structures. As shown in Fig. 1b and c, the checkerboard unit is made up of two or four isotropic materials, which determine the types and number of function combinations possible for thermal and electric fields. By rotating the even-numbered layers of the checkerboard structure, continuous function adjustment can be achieved. The geometry of the structure also determines the type of function combination that occurs during the rotation process. By controlling the spatial distribution and rotation time of the checkerboard unit, we can manipulate both thermal and electric fields.

The effective thermal and electric conductivities of the checkerboard determine the thermal and electric currents in the central region. According to the Keller theorem [43–46] and effective medium theory [22, 47–49], the effective thermal and electrical conductivity of the

checkerboard structure in polar coordinates satisfy

$$\kappa_r \kappa_\theta = \kappa_1 \kappa_2, \quad \sigma_r \sigma_\theta = \sigma_1 \sigma_2, \tag{1}$$

where $\kappa_r(\sigma_r)$ and $\kappa_\theta(\sigma_\theta)$ are the effective radial and tangential thermal (electric) conductivities, $\kappa_1(\sigma_1)$ and $\kappa_2(\sigma_2)$ are the thermal (electric) conductivities of the two units that make up the checkerboard structure. We suppose that the thermal (electrical) conductivity of the two units satisfies $\kappa_1 \kappa_2 = \kappa_r \kappa_\theta = \kappa_b^2$ ($\sigma_1 \sigma_2 = \sigma_r \sigma_\theta = \sigma_b^2$). The product of the effective radial and tangential thermal (electrical) conductivities of the checkerboard structure is equal to the square of the background thermal (electrical) conductivity, so the background heat (electric) flow is not disturbed. The value of $\kappa_r / \kappa_\theta (\sigma_r / \sigma_\theta)$ affects the heat (electric) flow distribution in the central area.

(1) When $\kappa_r / \kappa_\theta < 1(\sigma_r / \sigma_\theta < 1)$, the heat (electric) flow bypasses the central area to achieve thermal (electric) cloaking. If $\kappa_r / \kappa_\theta (\sigma_r / \sigma_\theta)$ is zero, the cloaking effect is perfect.
(2) When $\kappa_r / \kappa_\theta = 1(\sigma_r \sigma_\theta = 1)$, the heat (electric) flow keeps unchanged in the central area to achieve thermal (electric) sensing.
(3) When $\kappa_r / \kappa_\theta > 1(\sigma_r / \sigma_\theta > 1)$, the heat (electric) flow is concentrated in the central area to achieve the effect of thermal (electric) concentrating.

Therefore, spatiotemporal function prediction is mainly based on calculating the effective radial and tangential thermal (electric) conductivities of the checkerboard structure.

We focus on checkerboard structures constructed with two or four materials. In Fig. 2a, we illustrate a checkerboard structure made up of two isotropic materials with constant thermal and electric conductivities. The even layers rotate clockwise, while the odd layers remain stationary. The red dotted line in Fig. 2a represents the fixed line, while the brown dotted line rotates clockwise. We define $\Delta\theta$ as the central
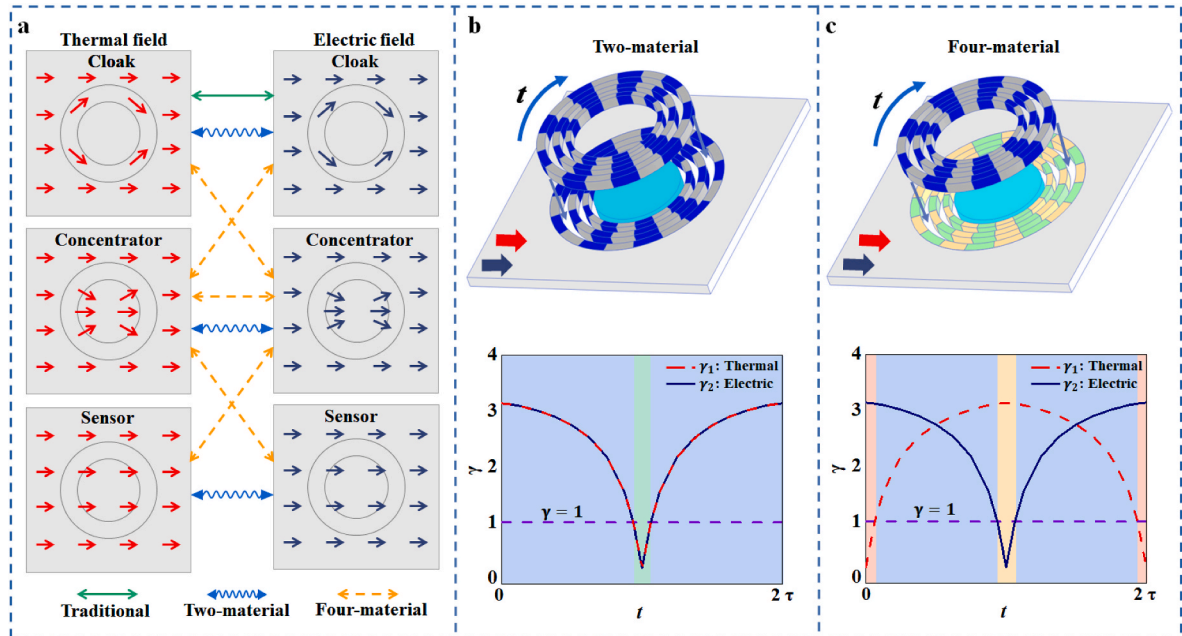

Fig. 1. Concept of spatiotemporal multiphysics metamaterials. A comparison is made between traditional schemes and our proposed scheme in (a). Traditional schemes only achieve one function combination, such as thermal cloaking plus electric cloaking. In contrast, our spatiotemporal multiphysics metamaterials, composed of two (or four) materials, can realize three (or five) function combinations. The two-material-based and four-material-based checkerboard structures are shown in (b) and (c), respectively. By rotating the even-numbered layers at a constant angular speed, the heat and electric currents in the central region can be altered, enabling continuous function adjustment. The rotation period is represented as 2τ, while the ratio of central flow density to background flow density is represented as γ. Thermal and electric fields are denoted as γ_1 and γ_2, respectively. If $\gamma_1 > 1(\gamma_2 > 1)$, the function achieved is thermal (electric) concentrating, meaning that the heat flow (current) in the central area is greater than in the background area. Conversely, if $\gamma_1 < 1(\gamma_2 < 1)$, the function is thermal (electric) cloaking. Finally, if $\gamma_1 = 1(\gamma_2 = 1)$, the function is thermal (electric) sensing. It's important to note that the heat and electric currents in the background remain unchanged during the rotation process.
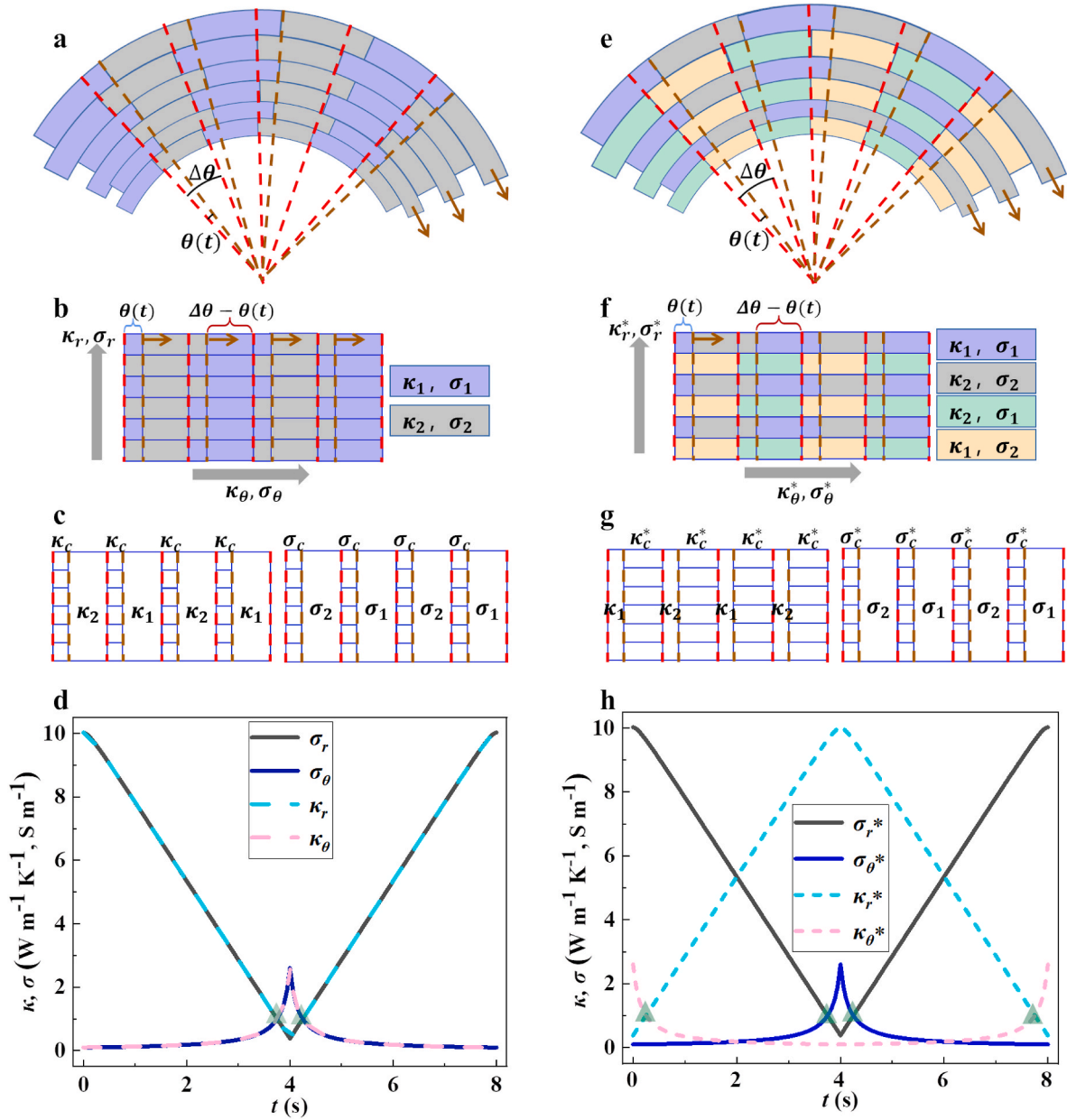
Fig. 2. Schematic diagram of spatiotemporal multiphysics metamaterials. (a) Two-material-based checkerboard structure. The brown arrows represent the rotation direction of even layers. (b) The checkerboard structure stretched from (a), regarded as a multilayer structure. (c) Separate display of thermal and electric conductivities. (d) Theoretical results of the structure in (a). (e)–(h) Similar to (a)–(d), and the difference is that the checkerboard structure consists of four materials. The function marked by the green triangles is sensing.

angle of a unit phase, and τ as the time it takes for the even-numbered layers to rotate $\Delta\theta$. The rotation angle $\theta(t)$ can be expressed as $\theta(t) = \Delta\theta t/\tau$. The position distribution of the checkerboard structure returns to its initial state after a rotation time of 2τ. Therefore, we consider only the rotating process within one period due to the periodicity of the checkerboard structure. By adjusting the angle $\theta(t)$, we can divide the sector area corresponding to a central angle $\Delta\theta$ into homogeneous and staggered phases. The homogeneous phase consists of units made of the same material, with thermal and electric conductivities of either (κ_1, σ_1) or (κ_2, σ_2). The staggered phase is composed of two isotropic material units, interlaced with thermal and electric conductivities of (κ_1, σ_1) and (κ_2, σ_2), respectively. During a period 2τ, the central angle corresponding to staggered phases is

$$
\theta_s(t) = \begin{cases} \dfrac{\Delta\theta}{\tau}t, & 0 < t < \tau \\[2ex] 2\Delta\theta - \dfrac{\Delta\theta}{\tau}t. & \tau < t < 2\tau \end{cases} \tag{2}
$$

During $0 < t < \tau$, the angle $\theta_s(t)$ increases, and during $\tau < t < 2\tau$, it decreases, with the checkerboard structure returning to its original state at 2τ, with no staggering phase. The effective thermal conductivity of the staggered phases is determined by the material and shape parameters of the two units [50]. The shape parameter of the staggered phases is a function of time and can be expressed as $\eta(t) = \ln(r_{i+1}/r_i)/\theta_s(t)$, where r_i is the radius of the i-th layer. To obtain the effective thermal conductivity κ_c of the staggered phases, we replace η in Equation (9) with $\eta(t)$ from Ref. [50]; please refer to Appendix A for the detailed derivation. In this way, the entire checkerboard structure can be viewed as consisting

of three homogeneous materials, with thermal conductivity values of κ_1, κ_c, and κ_2. Note that the thermal conductivity of the staggered phase κ_c differs between the tangential and radial directions.

We deform the fan-shaped structure in Fig. 2a into a multi-layer structure in Fig. 2b composed of staggered and homogeneous phases. The lateral thermal conductivity of the multi-layer structure is the tangential thermal conductivity of the fan-shaped structure, and the longitudinal thermal conductivity of the multi-layer structure is the radial thermal conductivity of the fan-shaped structure. The multi-layer structure can be approximated step-by-step using the effective medium theory to obtain the effective radial and tangential thermal conductivities of the rotatable checkerboard structure, please refer to Appendix B. The electric and thermal conductivities in the rotatable checkerboard structure can be separately considered to control the electric and thermal flow independently, as shown in Fig. 2c. Since the thermal and electric conductivities of the two-material checkerboard structure have the same variation, we only use thermal conductivity as an example for theoretical calculations and finally replace κ_1 and κ_2 with σ_1 and σ_2 to obtain the effective electric conductivity.

In order to provide clarity, we present in Fig. 2d the variation in effective thermal and electric conductivity of the rotatable checkerboard structure over one period 2τ, where $\tau = 4$s. The checkerboard structure comprises of two materials with parameters ($\kappa_1 = 20$ Wm^{-1}K^{-1}, $\sigma_1 = 20$ Sm^{-1}) and ($\kappa_2 = 0.05$ Wm^{-1}K^{-1}, $\sigma_2 = 0.05$ Sm^{-1}). The thermal and electric conductivities of the background and central regions are $\kappa_b = 1$ Wm^{-1}K^{-1} and $\sigma_b = 1$ Sm^{-1}. We have utilized Equations (A.6) and (A.7) from the Appendix to calculate the results shown in Fig. 2d. The dashed and solid lines represent thermal and electric conductivities, respectively. The overlap of the solid and dashed lines indicates that the thermal and electric conductivities satisfy the same equation. At $t = 3.75$ s and $t = 4.25$ s, the effective radial and tangential thermal (electric) conductivities are identical, indicating the thermal (electric) sensing function. The radial thermal (electric) conductivity is larger than the tangential thermal (electric) conductivity at 0 s $< t < 3.75$ s and 4.25 s $< t < 8$ s, which means that $\kappa_r/\kappa_\theta > 1(\sigma_r/\sigma_\theta > 1)$, demonstrating the thermal (electric) concentrating function. The radial thermal (electric) conductivity is smaller than the tangential thermal (electric) conductivity at 3.75 s $< t < 4.25$ s, indicating that $\kappa_r/\kappa_\theta < 1(\sigma_r/\sigma_\theta < 1)$ and demonstrating the thermal (electric) cloaking function. The thermal and electric fields of the two-material-based checkerboard structures have the same function and can be continuously regulated over time, resulting in spatiotemporal multiphysics metamaterials composed of two materials that realize three function combinations. If we consider using natural materials such as aluminum and nickel to construct a chessboard structure, the transformation rules for both thermal and electrical fields are still the same and can generate the three functions of concentrator, sensor, and cloak in the same order. The only difference is that the timing of the appearance of the sensor function in the thermal and electrical fields cannot be precisely the same (see details in Fig. A.2a-b).

Furthermore, we can also switch the thermal and electric functions with different rules. As depicted in Fig. 2e, we design a checkerboard structure comprising four isotropic materials. The parameters of these four materials are (κ_1, σ_1), (κ_1, σ_2), (κ_2, σ_1), and (κ_2, σ_2). From the structures shown in Fig. 2c and g, the electric conductivities of the checkerboard structures composed of two and four isotropic materials exhibit the same changes. Consequently, the effective electric conductivities of the checkerboard structures of these two configurations are identical. However, the thermal conductivity of the four-material-based checkerboard structure is different from that of the two-material-based checkerboard structure. The center angle corresponding to the staggered phase is

$$\theta_s^*(t) = \begin{cases} \Delta\theta - \dfrac{\Delta\theta}{\tau}t, & 0 < t < \tau \\ \dfrac{\Delta\theta}{\tau}t - \Delta\theta. & \tau < t < 2\tau \end{cases} \tag{3}$$

We replace all $\theta_s(t)$ in the thermal conductivity calculation of the two-material-based checkerboard structure with $\theta_s^*(t)$. Then, the effective thermal conductivity of the four-material-based checkerboard structure can be obtained (see Appendix C for detailed derivation).

Fig. 2h displays the effective thermal and electric conductivities as a function of time for the four-material-based checkerboard structure, as described by the parameters (κ_1, σ_1), (κ_1, σ_2), (κ_2, σ_1), and (κ_2, σ_2) with $\kappa_1 = 20$ Wm^{-1}K^{-1}, $\sigma_1 = 20$ Sm^{-1}, $\kappa_2 = 0.05$ Wm^{-1}K^{-1}, and $\sigma_2 = 0.05$ Sm^{-1}. By substituting these parameters into Equations (A.7) and (A.12) of the Appendix, we generate the results shown in Fig. 2h. Our theoretical predictions suggest that the four-material-based checkerboard structure can achieve five different function combinations. Specifically, we can achieve thermal sensing plus electric concentrating at $t = 0.25$ s and $t = 7.75$ s, thermal concentrating plus electric sensing at $t = 3.75$ s and $t = 4.25$ s, and thermal cloaking plus electric concentrating before 0.25 s and after 7.75 s. Additionally, we can achieve thermal concentrating plus electric cloaking during 3.75 s $< t < 4.25$ s, while the function combination at all other times is thermal concentrating plus electric concentrating. Thus, spatiotemporal multiphysics metamaterials composed of four materials can realize these five distinct function combinations. If we choose natural materials to construct the chessboard structure, the limitations of the κ/σ ratio of the natural materials will limit the functionality of the electric field. If the κ/σ of the two materials differ significantly, it will affect the appearance of the cloak and sensor functions. For details, please refer to Appendix E. Discussing the κ/σ ratio of materials can help us choose natural materials to form the chessboard structure. Consider a chessboard structure composed of natural materials such as nickel-iron alloy, tungsten, semiconductor material, and germanium. The transformation rules for thermal and electric fields are consistent with Fig. 2h and can generate five functional combinations in the same order (see details in Fig. A.2c-d). Therefore, our chessboard structure is also applicable to natural materials.

2.2. Simulation verification

We conduct finite-element simulations to verify the functionality of spatiotemporal multiphysics metamaterials. Initially, we consider a rotatable checkerboard structure composed of two isotropic materials. The hollow cylinder consisted of 15 sub-layers, with each layer being divided into 24 fan-shaped unit cells that are alternately arranged by the two isotropic materials. Even-numbered layers of this hollow cylinder rotated clockwise with time, as shown in Fig. 2a. We calculate the radius r_i of each layer using the formula $\ln(r_{i+1}/r_i) = \eta\Delta\theta$, with a shape parameter of $\eta = 1/\sqrt{10}$, and an inner diameter of $r_1 = 4$ cm, and a unit center angle of $\Delta\theta = 2\Pi/24$. We embed the checkerboard structure into a square with a side length of 45 cm and ignore the thermal impedance between the checkerboard structural units. We introduce 'Heat Transfer in Solids' module and 'Electric Currents' module into the two-dimensional system to simulate electric field and thermal field distribution. Temperature and potential differences are applied at the left and right boundaries to induce heat and electric currents through the entire structure. Specifically, we set the left boundary temperature and potential at 373 K and 10 mV, respectively, and the right boundary at 273 K and 0 mV. The thermal and electric conductivities of the entire spatiotemporal metamaterial are consistent with the theoretical predictions. The rotation period is $2\tau = 8$ s. In practice, we can connect and fix the even layers of the chessboard structure to a tray, and connect the tray to an external rotator. By setting the rotation speed, the rotor will cause the even layers of the chessboard structure to rotate simultaneously, resulting in a change in the configuration of the entire chessboard structure over time. During the rotation of the chessboard structure, our rotation speed is very slow, and the thermal diffusion length $L = \sqrt{\kappa t/(\rho C)}$ is much larger than the structure size. Therefore, each moment of the simulation is regarded as quasi-steady state.

The proposed theory enables the prediction of thermal and electric fields' functions at any given time. Spatiotemporal multiphysics metamaterials composed of two materials can realize three different function combinations, as shown in Fig. 3. To demonstrate this, we select three moments corresponding to the chessboard structure of three function combinations in simulations: $t = 0$ s, $t = 3.75$ s, and $t = 4$ s. In the theoretical diagram Fig. 2d, these three moments correspond to concentrating, sensing, and cloaking, respectively. At any time, the background isotherms and equipotential lines remain unchanged, indicating that the background heat and electric currents are not disturbed. At the initial time, the even-numbered layers have not yet started to rotate, and the checkerboard structure is composed of two uniform fan-shaped structures interlaced. The simulation results demonstrate the effect of thermal and electric concentrating. The heat and electric currents are concentrated in the central region without disturbing the background fields. In Fig. 3j and k, the temperature and electric potential gradients in the central region are more significant than in the background, proving the function combination of thermal plus electric concentrating. At $t = 3.75$ s, the isotherm and equipotential line spacing in the central area is consistent with the background. In Fig. 3j and k, the temperature and potential gradients in the central region are the same as the background, corresponding to thermal sensing plus electric sensing. At $t = 4$ s, the entire checkerboard structure consists of two materials interleaved. The simulation results show that neither the isotherm nor the equipotential line enters the central region. The temperature and potential gradients in the central region are close to zero. Heat and electric currents do not enter the central area, achieving the effect of thermal cloaking plus electric cloaking. See Fig. 3j and k. The isotherms and equipotential lines of zone II of the spatiotemporal metamaterial at $t = 4$ s are less smooth than those at $t = 3.75$ s because, at $t = 3.75$ s, the thermal and electric fields pass through a uniform region of thermal conductivity and electric conductivity in the radial direction. At $t = 4$ s, there is no uniform region; it is all an alternating region. These three function combinations can also be achieved from 4 s to 8 s, but the function switch direction is opposite from 0 s to 4 s (see Appendix F for

simulation results). Within a whole period of 8 s, the heat and electric flows in the central region of the checkerboard structure gradually decrease from a value higher than the background to zero and then gradually increase back to the initial state. We utilize a rotatable checkerboard structure to achieve time-responsive continuous adjustment of the thermal and electric functions. Thus, we verify the theory's reliability through simulations and demonstrate that spatiotemporal multiphysics metamaterials composed of two materials can achieve three different function combinations.

Thermal and electric fields can serve different functions. We propose a checkerboard structure made up of four isotropic materials with parameters consistent with Fig. 2h. We present simulation results at five key moments in Fig. 4: 0s, 0.25s, 2 s, 3.75 s, and 4 s. The left boundary temperature and potential are set at 373 K and 10 mV, and the right boundary is set at 273 K and 0 mV. No heat or electric flow is disturbed in the background region at any time. At $t = 0$ s, the heat flow bypasses the central area while the current concentrates, corresponding to thermal cloaking plus electric concentrating. At $t = 4$ s, the current bypasses the central region while the heat flow focuses, corresponding to electric cloaking plus thermal concentrating. We achieve thermal sensing plus electric concentrating at $t = 0.25$ s and thermal concentrating plus electric sensing at $t = 3.75$ s. The simulation results confirm that the theoretical predictions are indeed achieved. At $t = 2$ s, the even-numbered layers in the checkerboard structure rotate half the center corner of the unit. At this time, the radial thermal (electric) conductivity is higher than the tangential one, as shown in Fig. 2h. Both current and heat flows are concentrated in the central region, corresponding to thermal concentrating plus electric concentrating. As per Fig. 2h, thermal and electric concentrating is achieved from 0.25s to 3.75s. Thus, spatiotemporal multiphysics metamaterials made up of four materials can achieve five function combinations. From 4 s to 8 s, these five function combinations can also be implemented (see Appendix G for simulation results). Our design enables multi-field and multi-function operation with just time control, which substantially weakens the limitations of fixed functions.
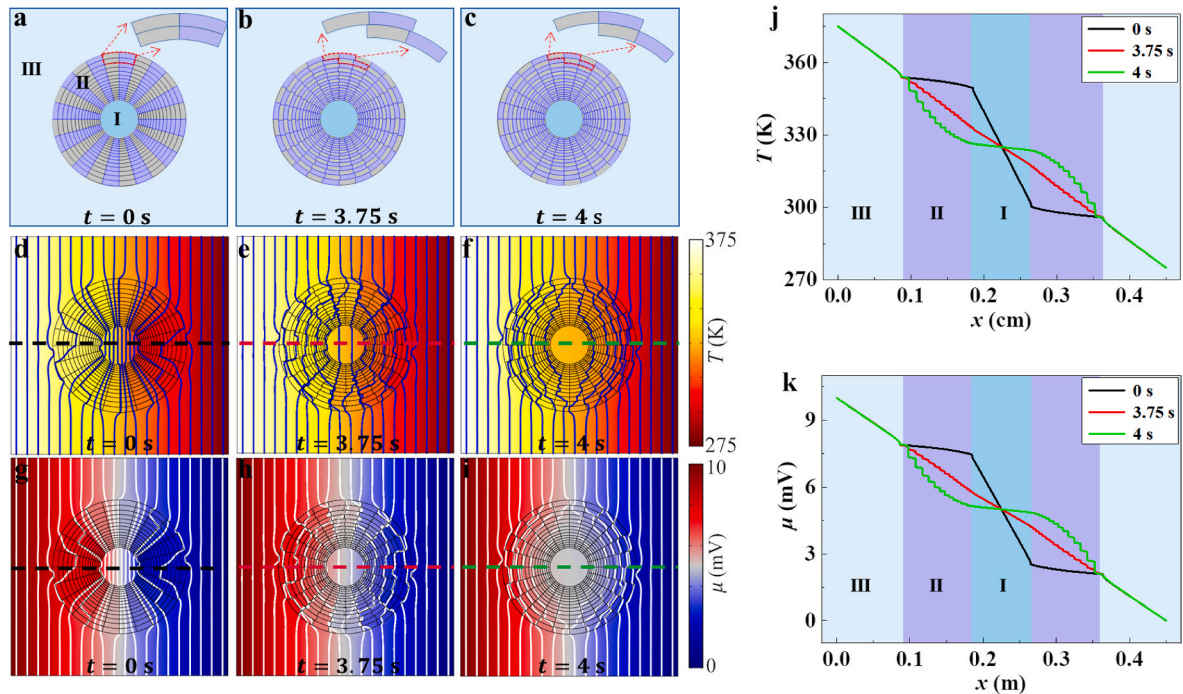

Fig. 3. Schematic diagrams and simulation results of a two-material-based checkerboard structure. (a)–(c) Structures with $t = 0$ s, $t = 3.75$ s, and $t = 4$ s. I, II, and III represent the central, checkerboard, and background areas. (d)–(f) Simulation results of the thermal field. Blue lines represent isotherms. (g)–(i) Simulation results of the electric field. White lines represent equipotential lines. (j) and (k) Data of the horizontal centerline from the simulation results in (d)–(f) and (g)–(i). The three temperature (or potential) lines in region III coincide.
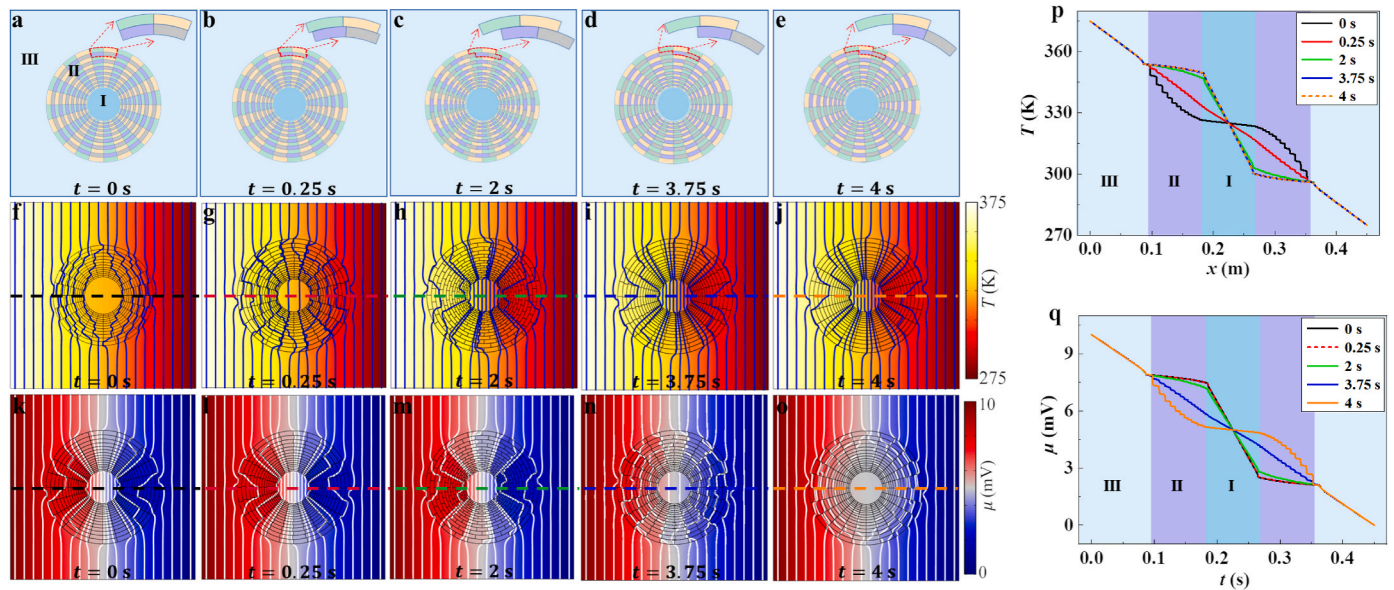
Fig. 4. Schematic diagrams and simulation results of a four-material-based checkerboard structure. (a)–(e) Structures with $t = 0$ s, $t = 0.25$ s, $t = 2$ s, $t = 3.75$ s, and $t = 4$ s. (f)–(j) Simulation results of the thermal field. (k)–(o) Simulation results of the electric field. (p) and (q) Data of the horizontal centerline from the simulation results in (f)–(j) and (k)–(o). The five temperature (or potential) lines in region III coincide.

Spatiotemporal multiphysics metamaterials can manipulate thermal and electric functions by altering the geometry of the checkerboard structure unit. The geometric parameters affect the number of possible function combinations of thermal and electric fields. For instance, we study a checkerboard structure composed of two isotropic materials and conduct simulations using shape parameters of $\eta = 1$ and $\eta = 1.5$ (refer to Appendix H for simulation results). The shape parameter $\eta = [\ln(r_{i+1}/r_i)]/(\Delta\theta)$ is solely dependent on the unit shape and not on time. A rotatable checkerboard structure with a shape parameter of $\eta = 1.5$ produces only one function combination, namely thermal and electric concentration. On the other hand, the rotatable checkerboard structure with a shape parameter of $\eta = 1$ combines thermal and electric sensing at $t = 4$ s, whereas during the remaining time, it concentrates both thermal and electric fields. The key difference between these two structures is that the concentrating degree of the first type diminishes to zero, whereas the second type does not. These two structures can repeatedly perform the process of concentration degree from high to low and back to high for an extended period, thus enabling timed heating and insulation. By setting the period to keep the object at a higher temperature, the object can be heated repeatedly. Similarly, the design can focus the current to maintain a high current density in a specific region. Therefore, spatiotemporal multiphysics metamaterials can adjust the function combinations by using various structure shapes.

3. Conclusions

In summary, our propose spatiotemporal multiphysics metamaterial features a rotatable checkerboard structure that can simultaneously regulate both thermal and electric fields. By introducing a temporal dimension, specifically the rotation time, we can continuously control the effective thermal and electric conductivities, which allows for function switching of thermal and electric fields. The spatiotemporal

checkerboard structure, made up of two or four materials, can achieve three or five function combinations, respectively, which demonstrates incredible performance. We utilize the time-dependent effective medium theory to predict real-time thermal and electric functions, which we confirm through simulations. Our design is robust, as only isotropic materials are needed to achieve multiple function combinations. This method could also be applied to other multiphysics fields, such as electromagnetic-acoustic and thermal-magnetic fields.

Author contribution

Min Lei: Formal analysis, Writing – original draft. Liujun Xu: Conceptualization, Formal analysis, Writing – review & editing, Jiping Huang: Conceptualization, Formal analysis, Writing – review & editing

Declaration of competing interest

The authors declare that they have no known competing financial interests or personal relationships that could have appeared to influence the work reported in this paper.

Data availability

Data will be made available on request.

Appendix I. Supplementary data

Supplementary data to this article can be found online at https://doi.org/10.1016/j.mtphys.2023.101057.

Appendix A. Calculation of the effective thermal conductivity of the staggered phases of two-material-based checkerboard structures

The effective thermal conductivity of a checkerboard structure consisting entirely of staggered phases (i.e., the rotating checkerboard structure at $\theta(t) = \Delta\theta$) is [50].

$$\kappa_{cr} = \begin{cases} \sqrt{\kappa_1\kappa_2}\left[\left(1 - \dfrac{2\sqrt{\kappa_1\kappa_2}}{\kappa_1+\kappa_2}\right)(\eta-1)+1\right], & \eta \leq 1 \\[4mm] \dfrac{\sqrt{\kappa_1\kappa_2}}{\left(1-\dfrac{2\sqrt{\kappa_1\kappa_2}}{\kappa_1+\kappa_2}\right)\left(\dfrac{1}{\eta}-1\right)+1}, & \eta \geq 1 \end{cases}$$

$$\kappa_{c\theta} = \begin{cases} \dfrac{\sqrt{\kappa_1\kappa_2}}{\left(1-\dfrac{2\sqrt{\kappa_1\kappa_2}}{\kappa_1+\kappa_2}\right)(\eta-1)+1}, & \eta \leq 1 \\[4mm] \sqrt{\kappa_1\kappa_2}\left[\left(1 - \dfrac{2\sqrt{\kappa_1\kappa_2}}{\kappa_1+\kappa_2}\right)\left(\dfrac{1}{\eta}-1\right)+1\right], & \eta \geq 1 \end{cases}$$

(A.1)

where shape parameter $\eta = \ln(r_{i+1}/r_i)/\Delta\theta$ is only related to the geometry of the checkerboard structure, independent of time. We replace $\Delta\theta$ with $\theta_s(t)$ to get the shape parameter of the staggered phase over time, which can be written as

$$\eta(t) = \ln(r_{i+1}/r_i)\Big/\theta_s(t) = \begin{cases} \eta\dfrac{\tau}{t}, & 0 < t < \tau \\[4mm] \eta\dfrac{\tau}{2\tau - t} & \tau < t < 2\tau \end{cases}$$

(A.2)

The shape parameter here is not only related to the unit shape of the checkerboard but also related to time. The new shape parameter is taken into Equation (A.1) to get the effective thermal conductivity κ_c of staggered phases. In polar coordinates, κ_c can be divided into radial thermal conductivity κ_{cr} and tangential thermal conductivity $\kappa_{c\theta}$, respectively,

$$\kappa_{cr} = \begin{cases} \dfrac{\sqrt{\kappa_1\kappa_2}}{\left(1-\dfrac{2\sqrt{\kappa_1\kappa_2}}{\kappa_1+\kappa_2}\right)\left(\dfrac{t}{\eta\tau}-1\right)+1}, & 0 \leq t \leq \eta\tau \\[4mm] \sqrt{\kappa_1\kappa_2}\left[\left(1-\dfrac{2\sqrt{\kappa_1\kappa_2}}{\kappa_1+\kappa_2}\right)\left(\dfrac{\eta\tau}{t}-1\right)+1\right], & \eta\tau \leq t \leq \tau \\[4mm] \sqrt{\kappa_1\kappa_2}\left[\left(1-\dfrac{2\sqrt{\kappa_1\kappa_2}}{\kappa_1+\kappa_2}\right)\left(\dfrac{\eta\tau}{2\tau-t}-1\right)+1\right], & \tau \leq t \leq (2-\eta)\tau \\[4mm] \dfrac{\sqrt{\kappa_1\kappa_2}}{\left(1-\dfrac{2\sqrt{\kappa_1\kappa_2}}{\kappa_1+\kappa_2}\right)\left(\dfrac{2\tau-t}{\eta\tau}-1\right)+1}, & (2-\eta)\tau \leq t \leq 2\tau \end{cases}$$

(A.3)

$$\kappa_{c\theta} = \begin{cases} \sqrt{\kappa_1\kappa_2}\left[\left(1-\dfrac{2\sqrt{\kappa_1\kappa_2}}{\kappa_1+\kappa_2}\right)\left(\dfrac{t}{\eta\tau}-1\right)+1\right], & 0 \leq t \leq \eta\tau \\[4mm] \dfrac{\sqrt{\kappa_1\kappa_2}}{\left(1-\dfrac{2\sqrt{\kappa_1\kappa_2}}{\kappa_1+\kappa_2}\right)\left(\dfrac{\eta\tau}{t}-1\right)+1}, & \eta\tau \leq t \leq \tau \\[4mm] \dfrac{\sqrt{\kappa_1\kappa_2}}{\left(1-\dfrac{2\sqrt{\kappa_1\kappa_2}}{\kappa_1+\kappa_2}\right)\left(\dfrac{\eta\tau}{2\tau-t}-1\right)+1}, & \tau \leq t \leq (2-\eta)\tau \\[4mm] \sqrt{\kappa_1\kappa_2}\left[\left(1-\dfrac{2\sqrt{\kappa_1\kappa_2}}{\kappa_1+\kappa_2}\right)\left(\dfrac{2\tau-t}{\eta\tau}-1\right)+1\right]. & (2-\eta)\tau \leq t \leq 2\tau \end{cases}$$

The effective radial and tangential thermal conductivity of the staggered phase over the entire period 2τ is composed of segmentation functions, which is a function of time. The effective thermal conductivity of the interleaved phase is also related to the shape parameter η of the checkerboard structure unit, and Equation (A.3) gives the result of $\eta \leq 1$. If $\eta > 1$, it is easy to remove the piecewise function with a contradictory time range in Equation (A.3).

Appendix B. Calculation of the effective thermal conductivity of two-material-based checkerboard structures
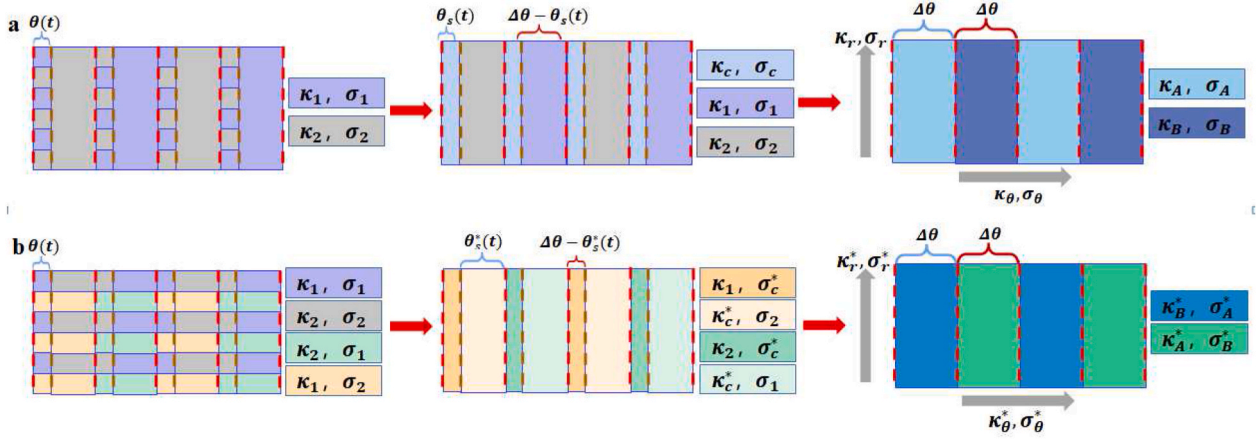

Fig. A.1. Evolution of rotatable checkerboard structures based on the effective medium theory. The rotatable checkerboard structure consists of (a) two materials and (b) four materials.

The fan-shaped structure of the checkerboard structure is morphed into a multi-layered structure composed of staggered and homogeneous phases shown in Fig. A.1a. We can combine a staggered and homogeneous phase to form a unit. The thermal conductivity of the staggered phase is κ_c, and the thermal conductivity of the homogeneous phase can be κ_1 or κ_2. Therefore, we can obtain two kinds of units: the combination of κ_c and κ_1 and the combination of κ_c and κ_2. According to the effective medium theory, the radial and tangential effective thermal conductivity of these two units can be calculated by

$$\kappa_{Ar} = \frac{\theta_s(t)}{\Delta\theta}\kappa_{cr} + \frac{\Delta\theta - \theta_s(t)}{\Delta\theta}\kappa_2, \kappa_{Br} = \frac{\theta_s(t)}{\Delta\theta}\kappa_{cr} + \frac{\Delta\theta - \theta_s(t)}{\Delta\theta}\kappa_1.$$

$$\frac{1}{\kappa_{A\theta}} = \frac{\theta_s(t)}{\Delta\theta}\frac{1}{\kappa_{c\theta}} + \frac{\Delta\theta - \theta_s(t)}{\Delta\theta}\frac{1}{\kappa_2}, \frac{1}{\kappa_{B\theta}} = \frac{\theta_s(t)}{\Delta\theta}\frac{1}{\kappa_{c\theta}} + \frac{\Delta\theta - \theta_s(t)}{\Delta\theta}\frac{1}{\kappa_1}.$$

(A.4)

where $\theta_s(t)/\Delta\theta$ is the proportion of staggered phase in a unit, and $(\Delta\theta - \theta_s(t))/\Delta\theta$ corresponds to homogeneous phase. Then the whole structure can be regarded as a multi-layer structure composed of two kinds of units staggered. Using the effective medium theory again,

$$\kappa_r = \frac{\kappa_{Ar} + \kappa_{Br}}{2}$$

$$\frac{1}{\kappa_\theta} = \frac{1}{2\kappa_{A\theta}} + \frac{1}{2\kappa_{B\theta}}.$$

(A.5)

The corresponding central angles of two units A and B in the chessboard structure are the same. The radial and tangential effective thermal conductivities of the rotatable checkerboard structure composed of two isotropic materials can be obtained by solving Equations (A.3)-Equation (A.5), which can be written as

$$\kappa_r = \begin{cases} \dfrac{t}{\tau}\,\dfrac{\sqrt{\kappa_1\kappa_2}}{\left(1-\frac{2\sqrt{\kappa_1\kappa_2}}{\kappa_1+\kappa_2}\right)\left(\frac{t}{\eta\tau}-1\right)+1} + \left(\dfrac{1}{2}-\dfrac{t}{2\tau}\right)(\kappa_1+\kappa_2), & 0\le t\le\eta\tau \\[3mm] \dfrac{t}{\tau}\sqrt{\kappa_1\kappa_2}\left[\left(1-\frac{2\sqrt{\kappa_1\kappa_2}}{\kappa_1+\kappa_2}\right)\left(\eta\frac{\tau}{t}-1\right)+1\right] + \left(\dfrac{1}{2}-\dfrac{t}{2\tau}\right)(\kappa_1+\kappa_2), & \eta\tau\le t\le\tau \\[3mm] \left(2-\dfrac{t}{\tau}\right)\sqrt{\kappa_1\kappa_2}\left[\left(1-\frac{2\sqrt{\kappa_1\kappa_2}}{\kappa_1+\kappa_2}\right)\left(\frac{\eta\tau}{2\tau-t}-1\right)+1\right] + \left(\dfrac{t}{2\tau}-\dfrac{1}{2}\right)(\kappa_1+\kappa_2), & \tau\le t\le(2-\eta)\tau \\[3mm] \left(2-\dfrac{t}{\tau}\right)\dfrac{\sqrt{\kappa_1\kappa_2}}{\left(1-\frac{2\sqrt{\kappa_1\kappa_2}}{\kappa_1+\kappa_2}\right)\left(\frac{2\tau-t}{\eta\tau}-1\right)+1} + \left(\dfrac{t}{2\tau}-\dfrac{1}{2}\right)(\kappa_1+\kappa_2), & (2-\eta)\tau\le t\le2\tau \end{cases}$$

$$\kappa_\theta = \begin{cases} \dfrac{\kappa_1\kappa_2}{\dfrac{t}{\tau}\dfrac{\sqrt{\kappa_1\kappa_2}}{\left(1-\frac{2\sqrt{\kappa_1\kappa_2}}{\kappa_1+\kappa_2}\right)\left(\frac{t}{\eta\tau}-1\right)+1} + \left(\frac{1}{2}-\frac{t}{2\tau}\right)(\kappa_1+\kappa_2)}, & 0\le t\le\eta\tau \\[3mm] \dfrac{\kappa_1\kappa_2}{\sqrt{\kappa_1\kappa_2}\,\dfrac{t}{\tau}\left[\left(1-\frac{2\sqrt{\kappa_1\kappa_2}}{\kappa_1+\kappa_2}\right)\left(\frac{\eta\tau}{t}-1\right)+1\right] + \left(\frac{1}{2}-\frac{t}{2\tau}\right)(\kappa_1+\kappa_2)}, & \eta\tau\le t\le\tau \\[3mm] \dfrac{\kappa_1\kappa_2}{\left(2-\frac{t}{\tau}\right)\sqrt{\kappa_1\kappa_2}\left[\left(1-\frac{2\sqrt{\kappa_1\kappa_2}}{\kappa_1+\kappa_2}\right)\left(\frac{\eta\tau}{2\tau-t}-1\right)+1\right] + \left(\frac{t}{2\tau}-\frac{1}{2}\right)(\kappa_1+\kappa_2)}, & \tau\le t\le(2-\eta)\tau \\[3mm] \dfrac{\kappa_1\kappa_2}{\left(2-\frac{t}{\tau}\right)\dfrac{\sqrt{\kappa_1\kappa_2}}{\left(1-\frac{2\sqrt{\kappa_1\kappa_2}}{\kappa_1+\kappa_2}\right)\left(\frac{2\tau-t}{\eta\tau}-1\right)+1} + \left(\frac{t}{2\tau}-\frac{1}{2}\right)(\kappa_1+\kappa_2)}. & (2-\eta)\tau\le t\le2\tau \end{cases}$$

(A.6)

Similarly, the radial and tangential effective electric conductivities of the rotatable checkerboard structure composed of two isotropic materials can be written as

$$\sigma_r = \begin{cases} \dfrac{t}{\tau}\,\dfrac{\sqrt{\sigma_1\sigma_2}}{\left(1-\frac{2\sqrt{\sigma_1\sigma_2}}{\sigma_1+\sigma_2}\right)\left(\frac{t}{\eta\tau}-1\right)+1} + \left(\dfrac{1}{2}-\dfrac{t}{2\tau}\right)(\sigma_1+\sigma_2), & 0\le t\le\eta\tau \\[3mm] \dfrac{t}{\tau}\sqrt{\sigma_1\sigma_2}\left[\left(1-\frac{2\sqrt{\sigma_1\sigma_2}}{\sigma_1+\sigma_2}\right)\left(\eta\frac{\tau}{t}-1\right)+1\right] + \left(\dfrac{1}{2}-\dfrac{t}{2\tau}\right)(\sigma_1+\sigma_2), & \eta\tau\le t\le\tau \\[3mm] \left(2-\dfrac{t}{\tau}\right)\sqrt{\sigma_1\sigma_2}\left[\left(1-\frac{2\sqrt{\sigma_1\sigma_2}}{\sigma_1+\sigma_2}\right)\left(\eta\frac{\tau}{2\tau-t}-1\right)+1\right] + \left(\dfrac{t}{2\tau}-\dfrac{1}{2}\right)(\sigma_1+\sigma_2), & \tau\le t\le(2-\eta)\tau \\[3mm] \left(2-\dfrac{t}{\tau}\right)\dfrac{\sqrt{\sigma_1\sigma_2}}{\left(1-\frac{2\sqrt{\sigma_1\sigma_2}}{\sigma_1+\sigma_2}\right)\left(\frac{2\tau-t}{\eta\tau}-1\right)+1} + \left(\dfrac{t}{2\tau}-\dfrac{1}{2}\right)(\sigma_1+\sigma_2), & (2-\eta)\tau\le t\le2\tau \end{cases}$$

$$\sigma_\theta = \begin{cases} \dfrac{\sigma_1\sigma_2}{\dfrac{t}{\tau}\dfrac{\sqrt{\sigma_1\sigma_2}}{\left(1-\frac{2\sqrt{\sigma_1\sigma_2}}{\sigma_1+\sigma_2}\right)\left(\frac{t}{\eta\tau}-1\right)+1} + \left(\frac{1}{2}-\frac{t}{2\tau}\right)(\sigma_1+\sigma_2)}, & 0\le t\le\eta\tau \\[3mm] \dfrac{\sigma_1\sigma_2}{\dfrac{t}{\tau}\sqrt{\sigma_1\sigma_2}\left[\left(1-\frac{2\sqrt{\sigma_1\sigma_2}}{\sigma_1+\sigma_2}\right)\left(\eta\frac{\tau}{t}-1\right)+1\right] + \left(\frac{1}{2}-\frac{t}{2\tau}\right)(\sigma_1+\sigma_2)}, & \eta\tau\le t\le\tau \\[3mm] \dfrac{\sigma_1\sigma_2}{\left(2-\frac{t}{\tau}\right)\sqrt{\sigma_1\sigma_2}\left[\left(1-\frac{2\sqrt{\sigma_1\sigma_2}}{\sigma_1+\sigma_2}\right)\left(\eta\frac{\tau}{2\tau-t}-1\right)+1\right] + \left(\frac{t}{2\tau}-\frac{1}{2}\right)(\sigma_1+\sigma_2)}, & \tau\le t\le(2-\eta)\tau \\[3mm] \dfrac{\sigma_1\sigma_2}{\left(2-\frac{t}{\tau}\right)\dfrac{\sqrt{\sigma_1\sigma_2}}{\left(1-\frac{2\sqrt{\sigma_1\sigma_2}}{\sigma_1+\sigma_2}\right)\left(\frac{2\tau-t}{\eta\tau}-1\right)+1} + \left(\frac{t}{2\tau}-\frac{1}{2}\right)(\sigma_1+\sigma_2)}. & (2-\eta)\tau\le t\le2\tau \end{cases}$$

(A.7)

Equation (A.6) and Equation (A.7) indicates that the effective thermal conductivity and electric conductivity satisfy the relation $\kappa_r\kappa_\theta=\kappa_1\kappa_2$ and $\sigma_r\sigma_\theta=\sigma_1\sigma_2$, which is consistent with Equation (1) in the main text.

Appendix C. Calculation of the effective thermal and electric conductivities of four-material-based checkerboard structures

The electric conductivity of the checkerboard structure composed of two isotropic materials and the checkerboard structure composed of four isotropic materials satisfy the same change, as shown in Fig. A.1a and b. Thus, we can get the relationship $\sigma_r^* = \sigma_r$ and $\sigma_\theta^* = \sigma_\theta$. Next, we calculate the effective thermal conductivity of the four-material checkerboard structure. When the even-numbered layers rotate through the angle $\theta(t)$, the central angle corresponding to the staggered area is $\theta_s^*(t)$ of the main text. The corresponding shape parameters of the staggering area of the checkerboard structure of the four materials are rewritten as

$$\eta^*(t) = \ln(r_{i+1}/r_i) \bigg/ \theta_s^*(t) = \begin{cases} \eta \dfrac{\tau}{\tau - t}, & 0 < t < \tau \\ \eta \dfrac{\tau}{t - \tau} & \tau < t < 2\tau \end{cases} \tag{A.8}$$

The effective radial and tangential thermal conductivity of the interleaved phase obtained by bringing the new shape parameters Equation (A.8) into Equation (A.1) can be written as

$$\kappa_{cr}^* = \begin{cases} \sqrt{\kappa_1 \kappa_2}\left[\left(1 - \dfrac{2\sqrt{\kappa_1\kappa_2}}{\kappa_1+\kappa_2}\right)\left(\eta\dfrac{\tau}{\tau-t}-1\right)+1\right], & 0 \leq t \leq \tau(1-\eta) \\[3mm] \dfrac{\sqrt{\kappa_1\kappa_2}}{\left(1-\dfrac{2\sqrt{\kappa_1\kappa_2}}{\kappa_1+\kappa_2}\right)\left(\dfrac{\tau-t}{\eta\tau}-1\right)+1}, & \tau(1-\eta) \leq t \leq \tau \\[3mm] \dfrac{\sqrt{\kappa_1\kappa_2}}{\left(1-\dfrac{2\sqrt{\kappa_1\kappa_2}}{\kappa_1+\kappa_2}\right)\left(\dfrac{t-\tau}{\eta\tau}-1\right)+1}, & \tau \leq t \leq \tau(1+\eta) \\[3mm] \sqrt{\kappa_1\kappa_2}\left[\left(1-\dfrac{2\sqrt{\kappa_1\kappa_2}}{\kappa_1+\kappa_2}\right)\left(\eta\dfrac{\tau}{t-\tau}-1\right)+1\right], & \tau(1+\eta) \leq t \leq 2\tau \end{cases} \tag{A.9}$$

$$\kappa_{c\theta}^* = \begin{cases} \dfrac{\sqrt{\kappa_1\kappa_2}}{\left(1-\dfrac{2\sqrt{\kappa_1\kappa_2}}{\kappa_1+\kappa_2}\right)\left(\eta\dfrac{\tau}{\tau-t}-1\right)+1}, & 0 \leq t \leq \tau(1-\eta) \\[3mm] \sqrt{\kappa_1\kappa_2}\left[\left(1-\dfrac{2\sqrt{\kappa_1\kappa_2}}{\kappa_1+\kappa_2}\right)\left(\dfrac{\tau-t}{\eta\tau}-1\right)+1\right], & \tau(1-\eta) \leq t \leq \tau \\[3mm] \sqrt{\kappa_1\kappa_2}\left[\left(1-\dfrac{2\sqrt{\kappa_1\kappa_2}}{\kappa_1+\kappa_2}\right)\left(\dfrac{t-\tau}{\eta\tau}-1\right)+1\right], & \tau \leq t \leq \tau(1+\eta) \\[3mm] \dfrac{\sqrt{\kappa_1\kappa_2}}{\left(1-\dfrac{2\sqrt{\kappa_1\kappa_2}}{\kappa_1+\kappa_2}\right)\left(\eta\dfrac{\tau}{t-\tau}-1\right)+1}. & \tau(1+\eta) \leq t \leq 2\tau \end{cases}$$

Similar to the checkerboard structure of the two materials, κ_c^* is combined with κ_1 and κ_2, respectively. The entire checkerboard structure is regarded as the staggered composition of two elements A and B, whose thermal conductivity is written as

$$\kappa_{Ar}^* = \frac{\theta_s^*(t)}{\Delta\theta}\kappa_{cr}^* + \frac{\Delta\theta - \theta_s^*(t)}{\Delta\theta}\kappa_2, \kappa_{Br}^* = \frac{\theta_s^*(t)}{\Delta\theta}\kappa_{cr}^* + \frac{\Delta\theta - \theta_s^*(t)}{\Delta\theta}\kappa_1.$$

$$\frac{1}{\kappa_{A\theta}^*} = \frac{\theta_s^*(t)}{\Delta\theta}\frac{1}{\kappa_{c\theta}^*} + \frac{\Delta\theta - \theta_s^*(t)}{\Delta\theta}\frac{1}{\kappa_2}, \frac{1}{\kappa_{B\theta}^*} = \frac{\theta_s^*(t)}{\Delta\theta}\frac{1}{\kappa_{c\theta}^*} + \frac{\Delta\theta - \theta_s^*(t)}{\Delta\theta}\frac{1}{\kappa_1}. \tag{A.10}$$

Again using the effective medium theory, the effective thermal conductivity of the entire checkerboard structure can be obtained,

$$\kappa_r^* = \frac{\kappa_{Ar}^* + \kappa_{Br}^*}{2}$$

$$\frac{1}{\kappa_\theta^*} = \frac{1}{2\kappa_{A\theta}^*} + \frac{1}{2\kappa_{B\theta}^*}. \tag{A.11}$$

After calculation, the effective thermal conductivity of the rotatable checkerboard structure composed of four isotropic materials can be written as

$$\kappa_r^* = \begin{cases} \left(1-\dfrac{t}{\tau}\right)\sqrt{\kappa_1\kappa_2}\left[\left(1-\dfrac{2\sqrt{\kappa_1\kappa_2}}{\kappa_1+\kappa_2}\right)\left(\dfrac{\eta\tau}{\tau-t}-1\right)+1\right]+\dfrac{t}{2\tau}(\kappa_1+\kappa_2), & 0 \le t \le \tau(1-\eta) \\[3em] \left(1-\dfrac{t}{\tau}\right)\dfrac{\sqrt{\kappa_1\kappa_2}}{\left(1-\dfrac{2\sqrt{\kappa_1\kappa_2}}{\kappa_1+\kappa_2}\right)\left(\dfrac{\tau-t}{\eta\tau}-1\right)+1}+\dfrac{t}{2\tau}(\kappa_1+\kappa_2), & \tau(1-\eta) \le t \le \tau \\[3em] \left(\dfrac{t}{\tau}-1\right)\dfrac{\sqrt{\kappa_1\kappa_2}}{\left(1-\dfrac{2\sqrt{\kappa_1\kappa_2}}{\kappa_1+\kappa_2}\right)\left(\dfrac{t-\tau}{\eta\tau}-1\right)+1}+\left(1-\dfrac{t}{2\tau}\right)(\kappa_1+\kappa_2), & \tau \le t \le \tau(1+\eta) \\[3em] \left(\dfrac{t}{\tau}-1\right)\sqrt{\kappa_1\kappa_2}\left[\left(1-\dfrac{2\sqrt{\kappa_1\kappa_2}}{\kappa_1+\kappa_2}\right)\left(\dfrac{\eta\tau}{t-\tau}-1\right)+1\right]+\left(1-\dfrac{t}{2\tau}\right)(\kappa_1+\kappa_2), & \tau(1+\eta) \le t \le 2\tau \end{cases}$$

$$\kappa_\theta^* = \begin{cases} \dfrac{\kappa_1\kappa_2}{\left(1-\dfrac{t}{\tau}\right)\sqrt{\kappa_1\kappa_2}\left[\left(1-\dfrac{2\sqrt{\kappa_1\kappa_2}}{\kappa_1+\kappa_2}\right)\left(\dfrac{\eta\tau}{\tau-t}-1\right)+1\right]+\dfrac{t}{2\tau}(\kappa_1+\kappa_2)}, & 0 \le t \le \tau(1-\eta) \\[3em] \dfrac{\kappa_1\kappa_2}{\left(1-\dfrac{t}{\tau}\right)\dfrac{\sqrt{\kappa_1\kappa_2}}{\left(1-\dfrac{2\sqrt{\kappa_1\kappa_2}}{\kappa_1+\kappa_2}\right)\left(\dfrac{\tau-t}{\eta\tau}-1\right)+1}+\dfrac{t}{2\tau}(\kappa_1+\kappa_2)}, & \tau(1-\eta) \le t \le \tau \\[3em] \dfrac{\kappa_1\kappa_2}{\left(\dfrac{t}{\tau}-1\right)\dfrac{\sqrt{\kappa_1\kappa_2}}{\left(1-\dfrac{2\sqrt{\kappa_1\kappa_2}}{\kappa_1+\kappa_2}\right)\left(\dfrac{t-\tau}{\eta\tau}-1\right)+1}+\left(1-\dfrac{t}{2\tau}\right)(\kappa_1+\kappa_2)}, & \tau \le t \le \tau(1+\eta) \\[3em] \dfrac{\kappa_1\kappa_2}{\left(\dfrac{t}{\tau}-1\right)\sqrt{\kappa_1\kappa_2}\left[\left(1-\dfrac{2\sqrt{\kappa_1\kappa_2}}{\kappa_1+\kappa_2}\right)\left(\dfrac{\eta\tau}{t-\tau}-1\right)+1\right]+\left(1-\dfrac{t}{2\tau}\right)(\kappa_1+\kappa_2)}, & \tau(1+\eta) \le t \le 2\tau \end{cases}$$

$$(A.12)$$

Appendix D. Chessboard structures composed of two natural materials and four natural materials

We demonstrate a chessboard structure composed of aluminum ($\kappa_1 = 237$ Wm^{-1}K^{-1}, $\sigma_1 = 3.3 \times 10^7$ Sm^{-1}) and nickel ($\kappa_2 = 90$ Wm^{-1}K^{-1}, $\sigma_2 = 6.8 \times 10^6$ Sm^{-1}), as shown in Fig. A.2a and 2b. The thermal concentrator occurs before 2.7 s and after 5.3 s, the thermal sensor occurs at 2.7 s and 5.3 s, and the thermal cloak occurs between 2.7 s and 5.3 s. The transformation rules for the electrical field are the same as those for the thermal field, except that the electrical sensor appears at 2.8 s and 5.2 s. When using natural materials, the thermal and electrical sensors will not appear at the same time, and the three combinations of functions in the main text will become four. The combination of thermal plus electric sensors disappears, while the combinations of thermal sensor plus electric concentrator and thermal cloak plus electric sensor will appear. Consider a chessboard structure composed of two natural materials with significant differences: copper ($\kappa_1 = 401$ Wm^{-1}K^{-1}, $\sigma_1 = 5.96 \times 10^7$ Sm^{-1}) and Acrylonitrile-butadiene-styrene ($\kappa_2 = 0.2$ Wm^{-1}K^{-1}, $\sigma_2 = 1 \times 10^{-7}$ Sm^{-1}). In the thermal field, the sensor occurs at 3.88 s and 4.12 s, while in the electric field, the sensor occurs at 3.99 s and 4.01 s. The transformation rules are consistent with Fig. A.2a and 2b, except that the cloak appears for a very short time. We can choose suitable natural materials to construct the chessboard structure according to practical needs.

Taking the example of a chessboard structure composed of nickel-iron alloy ($\kappa_2 = 10$ Wm^{-1}K^{-1}, $\sigma_1 = 1.4 \times 10^6$ Sm^{-1}), tungsten ($\kappa_1 = 150$ Wm^{-1}K^{-1}, $\sigma_1 = 1.4 \times 10^6$ Sm^{-1}), semiconductor material ($\kappa_1 = 150$ Wm^{-1}K^{-1}, $\sigma_2 = 100$ Sm^{-1}), and germanium ($\kappa_2 = 10$ Wm^{-1}K^{-1}, $\sigma_2 = 100$ Sm^{-1}). as shown in Fig. A.2c and 2d. The chessboard structure composed of four natural materials also exhibits five functional combinations, in the same order as those in the main text. However, due to the significant differences in the parameters of the four natural materials, the timing of the appearance of each functional combination will be significantly different. The transformation rules and functional combinations of the chessboard structure composed of four natural materials are the same as Fig. 2h in the main text.
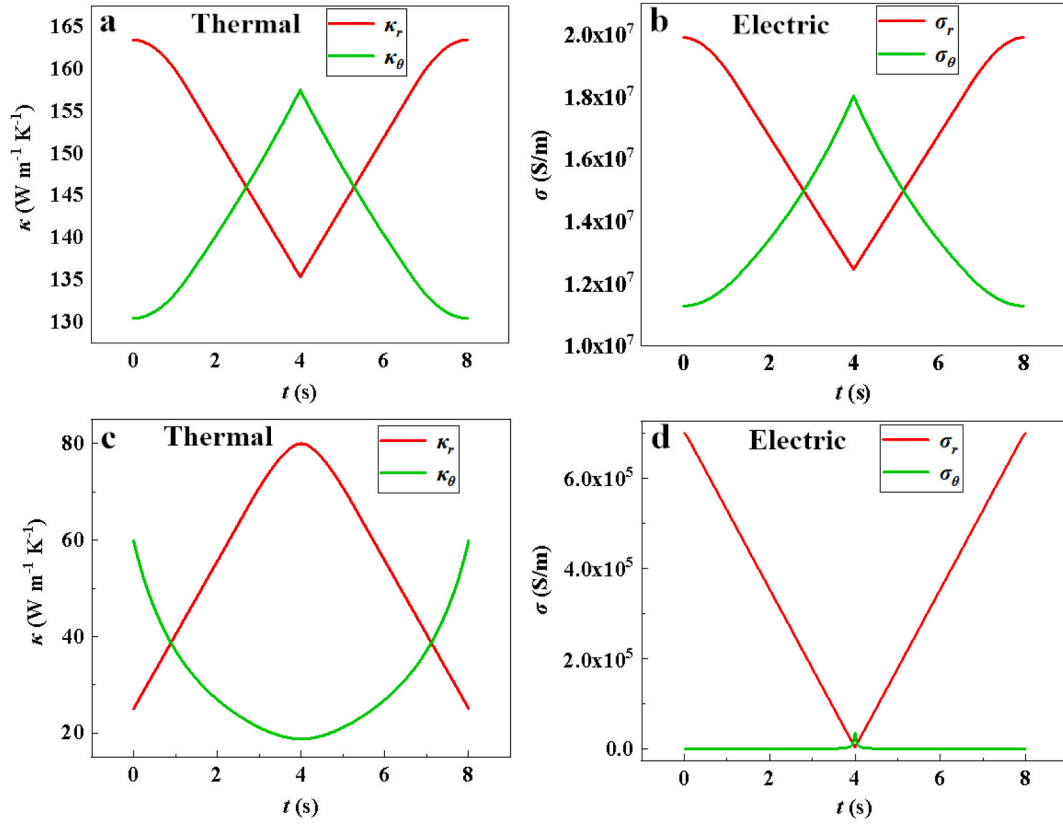
Fig. A.2. Theoretical schematic diagrams of chessboard structures composed of two natural materials and four natural materials. (a) and (b) Thermal conductivity and electrical conductivity distributions of a chessboard structure composed of aluminum and nickel. (c) and (d) Thermal conductivity and electrical conductivity distributions of a chessboard structure composed of nickel-iron alloy, tungsten, semiconductor material, and germanium.

Appendix E. Effect of κ/σ ratio of material on thermal and electric field functions

We use copper ($\kappa_1 = 400 \, \text{Wm}^{-1}\text{K}^{-1}$, $\sigma_1 = 6 \times 10^7 \, \text{Sm}^{-1}$) as material 1 to form the chessboard structure and discuss the impact of the κ/σ ratio of materials 2 and 3 on functionality. The thermal conductivity and electrical conductivity of materials 2 and 3 satisfy the relationship: $\kappa_1/\sigma_2 = \beta_1$, $\kappa_2/\sigma_1 = \beta_2$. By substituting the parameters β_1 and β_2 into Equation (A.7) and Equation (A.12), we calculate the variation of the effective electric conductivity and thermal conductivity of the chessboard structure with time, as shown in Fig. A.3. From Fig. A.3a, we can see that the cloak and sensor functions only appear when β_1 is around 10^{-3}. If β_1 is larger, only the cloak function will appear because the larger the β_1, the smaller the σ_2. If the difference between σ_2 and σ_1 is too large, the cloak function cannot appear. For the thermal field, three functions will appear between $\beta_2 = 10^{-10}$ and $\beta_2 = 10^{-6}$ (κ_2 between 10^{-3} and 10^1), and the order of appearance is not affected. Therefore, the κ/σ ratio will affect the functionality of the thermal and electric fields and even the appearance of electric cloaks and sensors.

In practice, the range of the κ/σ ratio of thermoelectric materials is also quite wide. The thermal conductivity of thermoelectric materials consists of electronic thermal conductivity and phonon thermal conductivity. The relationship between electronic thermal conductivity and electric conductivity satisfies the Wiedemann-Franz law: $\kappa_e = L\sigma T$, where L is the Lorenz constant. Phonon thermal conductivity is independent of conductivity. For some common metal materials, such as copper, silver, aluminum, their thermal conductivity is mainly composed of electronic thermal conductivity, and the κ/σ ratio is related to temperature. At room temperature, the order of magnitude is 10^{-6}. We can select metal materials as material 1. Insulating materials do not conduct electricity and mainly rely on phonon thermal conductivity to conduct heat. Therefore, the κ/σ ratio is very large, which can affect the occurrence of electric cloaks and electric sensors and is not suitable as a candidate for material 2. The thermal conductivity of semiconductor materials considers both electronic thermal conductivity and phonon thermal conductivity, and the κ/σ ratio is between that of metal and insulators, which can be used as material 2. Material 3 can be made up of some low thermal conductivity insulating materials, such as polyurethane. The selection of material 4 is related to the first three materials, $\kappa_2/\sigma_2 = \sigma_1\beta_1\beta_2/\kappa_1$. Some low thermal conductivity metal materials and semiconductor materials can be used. Therefore, the discussion of the κ/σ ratio can well predict the function and help to choose suitable materials to form the chessboard structure.
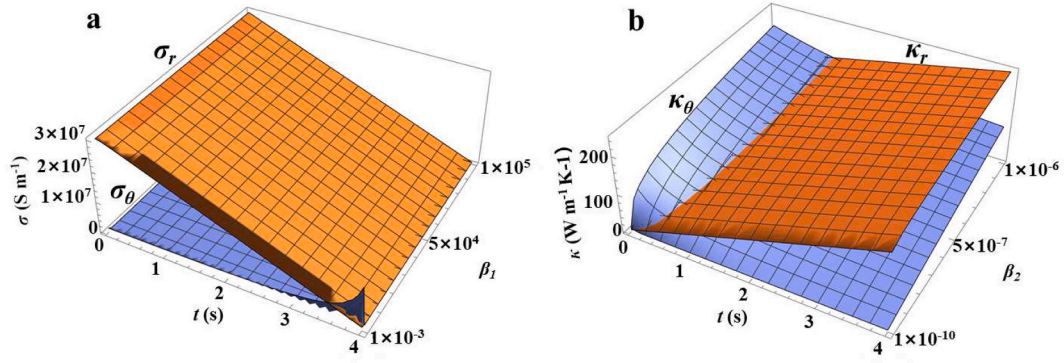
Fig. A.3. The effective electrical conductivity and thermal conductivity of the chessboard structure of four materials. Effect of κ/σ (i.e. β) value on the function of electric field (a) and thermal field (b).

Appendix F. Simulation results of two-material-based checkerboard structures during $\tau \leq t \leq 2\tau$
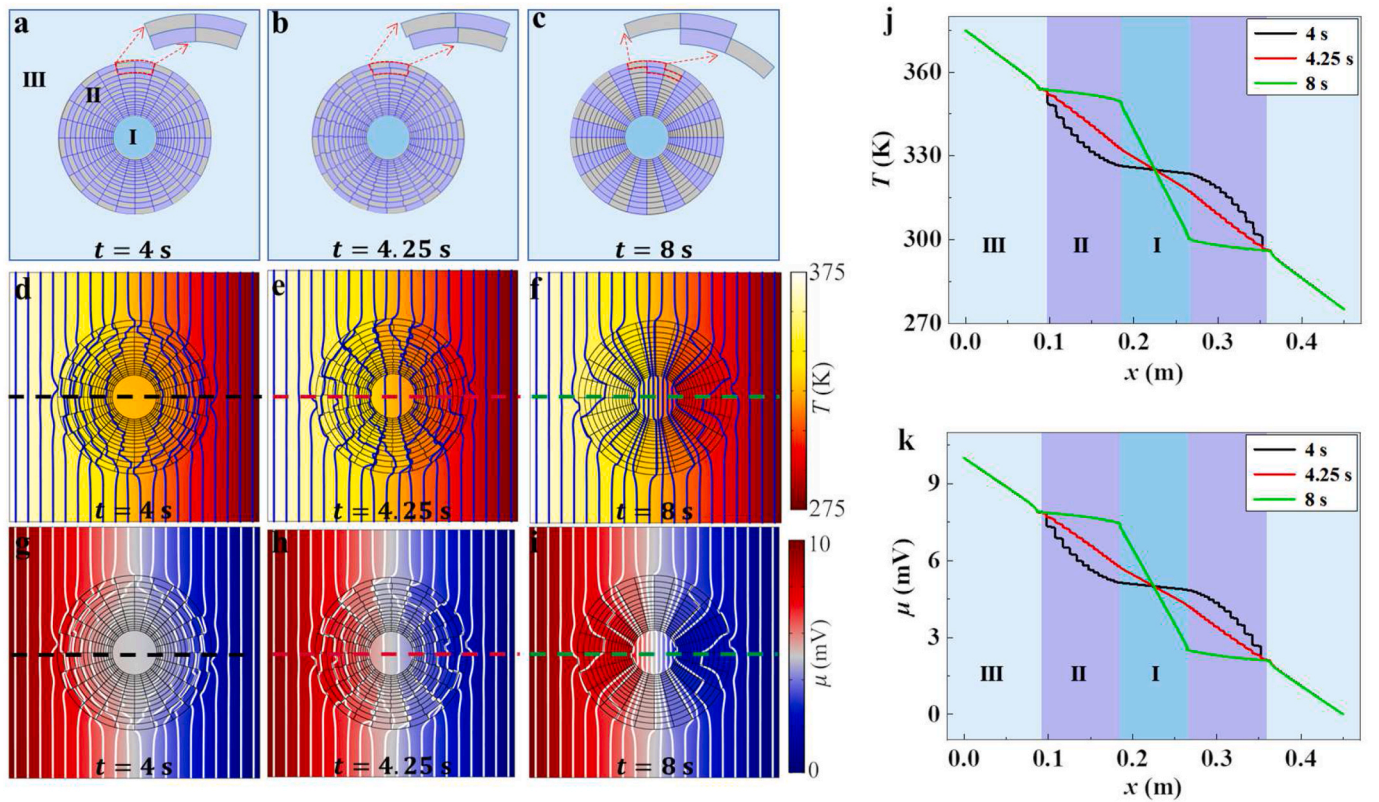

Fig. A.4. (a)–(c) Structures with $t = 4$ s, $t = 4.25$ s, $t = 8$ s. (d)–(f) and (g)–(i) Simulation results of the thermal and electric fields. (j) and (k) Data of the horizontal center line from the simulation results of (d)–(f) and (g)–(i). The three temperature (or potential) lines in region III coincide.

During the time period of 4 s $\leq t \leq$ 8 s, three functional combinations appear in two-material checkerboard structures, as shown in Fig. A.4. At $t = 4$ s, the functional combination is thermal cloak plus electric cloak. At $t = 4.25$ s, it changes to thermal sensor plus electric sensor. Finally, at $t = 8$ s, the functional combination becomes thermal concentrator plus electric concentrator. The functions of the thermal and electric fields shift from cloaks to sensors to concentrators over time. The direction of the functional change in the second half of the cycle is opposite to that in the first half.

Appendix G. Simulation results of four-material-based checkerboard structures during $\tau \leq t \leq 2\tau$

The checkerboard structure of four materials completes five functional combinations in time 4 s $\leq t \leq$ 8 s, as shown in Fig. A.5. With the increase of time, the concentration degree of the thermal concentrator gradually decreases to zero at $t = 7.75$ s, and the function becomes a sensor. The heat flow in the middle region continues to decline, finally changing function to cloak at $t = 8$ s. The direction of the phase transition of the electric field is opposite to that of the thermal field. The five function combinations obtained at these five moments are in agreement with the results predicted by the theory.
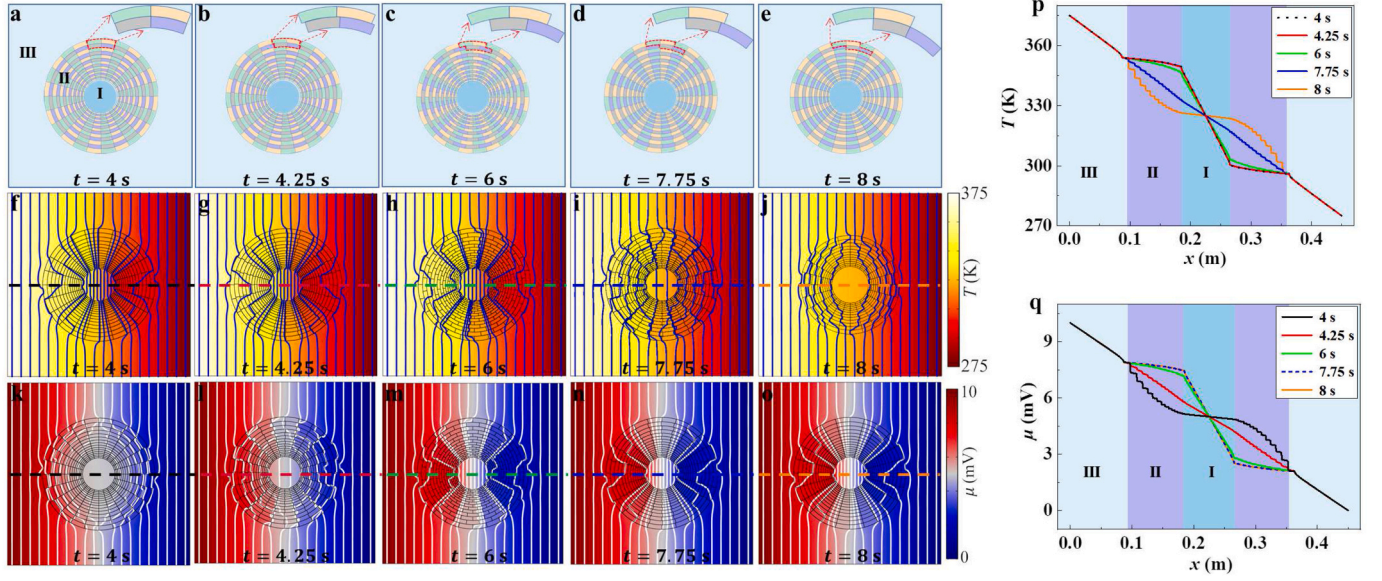
Fig. A.5. (a)–(e) Structures with $t = 4$ s, $t = 4.25$ s, $t = 6$ s, $t = 7.75$ s, $t = 8$ s. (f)–(j) and (k)–(o) Simulation results of the thermal and electric fields. (p) and (q) Data of the horizontal center line from the simulation results of (f)–(j) and (k)–(o). The five temperature (or potential) lines in region III coincide.

Appendix H. Theory and simulation results of checkerboard structures with different shapes

The checkerboard structure consists of two isotropic materials, with parameters of ($\kappa_1 = 10$ Wm^{-1}K^{-1}, $\sigma_1 = 10$ Sm^{-1}) and ($\kappa_2 = 0.1$ Wm^{-1}K^{-1}, $\sigma_2 = 0.1$ Sm^{-1}), respectively. To compare the radial and tangential thermal (electric) conductivity, we use η and t as independent variables in Equations (A.6) (Equations (A.7)). The remaining parameters are the same as in Fig. 3 of the main text. The phase diagram for the drawable function with η as the horizontal axis and t as the vertical axis is presented in Fig. A.6a, where $\tau = 4$ s represents half a period. Since the results for the second half period are symmetric to those of the first half period, it is sufficient to show the outcomes for one-half period. The blue area represents $\kappa_r/\kappa_\theta > 1$ ($\sigma_r/\sigma_\theta > 1$), corresponding to thermal concentration (electric concentration). The yellow area represents $\kappa_r/\kappa_\theta < 1$ ($\sigma_r/\sigma_\theta < 1$), corresponding to thermal cloak (electric cloak). The red line represents $\kappa_r/\kappa_\theta = 1$ ($\sigma_r/\sigma_\theta = 1$), corresponding to thermal sensor (electric sensor). The shape parameter affects the functional switching of the thermal and electric fields. When the shape parameter is $\eta = \ln(r_{i+1}/r_i)/\Delta\theta > 1$, the thermal and electric fields function as concentrators at any time. For a shape parameter $\eta < 1$, the thermal and electric field functions switch from concentrator to sensor to cloak over time. The thermal and electric fields transition from concentrator to sensor when $\eta = 1$, and the cloak effect does not appear. Therefore, we can use the shape parameter η to theoretically predict the type of function that will appear and when the function will switch.
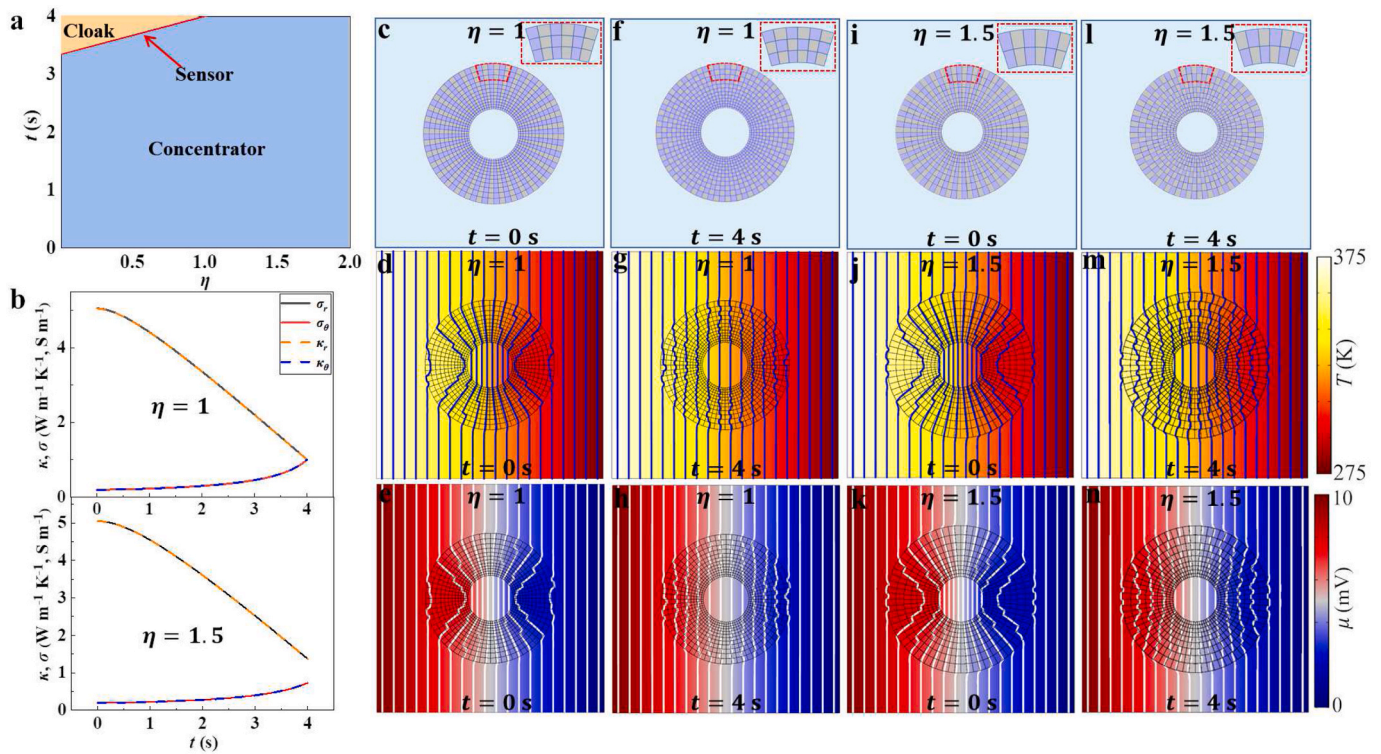
Fig. A.6. Simulation and theoretical results of checkerboard structures with different shapes. (a) Shape and time determine the phase diagrams of thermal and electric functions. (b) Variation of the effective thermal and electric conductivities with $\eta = 1$ and $\eta = 1.5$. (c)–(h) Structures and simulation results of the checkerboard structure with $\eta = 1$ at $t = 0$ s and $t = 4$ s. (i)–(n) Checkerboard structure with $\eta = 1.5$.

We select two checkerboard structures with shape parameters $\eta = 1$ and $\eta = 1.5$ for simulations. According to theory, we plot the time-dependent changes of the effective thermal and electric conductivity of both checkerboard structures, as shown in Fig. A.6b. Fig. A.6c-n shows the schematic diagram and simulation results of the rotatable checkerboard structure at $t = 0$ s and $t = 4$ s. For the checkerboard structure with $\eta = 1$, the ratio of the radial thermal (electric) conductivity to the tangential thermal (electric) conductivity is only $\kappa_r/\kappa_\theta = 1(\sigma_r/\sigma_\theta = 1)$ at $t = 4$ s, and $\kappa_r/\kappa_\theta > 1(\sigma_r/\sigma_\theta > 1)$ for the rest of the time. The simulation results show that the checkerboard structure achieves the function combination of thermal concentration plus electric concentration at $t = 0$ s and thermal sensor plus electric sensor at $t = 4$ s. For the rotatable checkerboard structure with shape parameter $\eta = 1.5$, the radial thermal (electric) conductivity is greater than the tangential thermal (electric) conductivity at any time, and thus the thermal and electric fields correspond to the function of the concentrator at any time. However, the degree of concentration achieved by these two structures is not constant but gradually decreases over time.

References

[1] M.Y. Gao, P. Wang, L.L. Jiang, B.W. Wang, Y. Yao, S. Liu, D.W. Chu, W.L. Cheng, Y. R. Lu, Power generation for wearable systems, Energy Environ. Sci. 14 (2021) 2114–2157, https://doi.org/10.1039/d0ee03911j.

[2] S.H. Fan, W. Li, Photonics and thermodynamics concepts in radiative cooling, Nat. Photonics 16 (2022) 182–190, https://doi.org/10.1038/s41566-021-00921-9.

[3] C.Y. Wang, Z. Vangelatos, C.P. Grigoropoulos, Z. Ma, Micro-engineered architected metamaterials for cell and tissue engineering, Mater, Today Adv 13 (2022): 100206, https://doi.org/10.1016/j.mtadv.2022.100206.

[4] Z. Ma, D. Zhao, C. She, Y. Yang, R. Yang, Personal thermal management techniques for thermal comfort and building energy saving, Mater. Today Phys. 20 (2021): 100465, https://doi.org/10.1016/j.mtphys.2021.100465.

[5] L. Xu, H.Y. Chen, Transformation metamaterials, Adv. Mater. 33 (2021): 2005489, https://doi.org/10.1002/adma.202005489.

[6] F. Martinez, M. Maldovan, Metamaterials: optical, acoustic, elastic, heat, mass, electric, magnetic, and hydrodynamic cloaking, Mater. Today Phys. 27 (2022): 100819, https://doi.org/10.1016/j.mtphys.2022.100819.

[7] Y.Z. Shi, Q.H. Song, I. Toftul, T.T. Zhu, Y.F. Yu, W.M. Zhu, D.P. Tsai, Y. Kivshar, A. Q. Liu, Optical manipulation with metamaterial structures, Appl. Phys. Rev. 9 (2022): 031303, https://doi.org/10.1063/5.0091280.

[8] H.R. Xue, Y.H. Yang, B.L. Zhang, Topological acoustics, Nat. Rev. Mater. 7 (2022) 974–990, https://doi.org/10.1038/s41578-022-00465-6.

[9] S. Yang, J. Wang, G.L. Dai, F.B. Yang, J.P. Huang, Controlling macroscopic heat transfer with thermal metamaterials: theory, experiment and application, Phys. Rep. 908 (2021) 1–65, https://doi.org/10.1016/j.physrep.2020.12.006.

[10] Z.R. Zhang, L.J. Xu, T. Qu, M. Lei, Z.K. Lin, X.P. Ouyang, J.H. Jiang, J.P. Huang, Diffusion metamaterials, Nat. Rev. Phys. (2023) in press.

[11] J. Park, J.R. Youn, Y.S. Song, Hydrodynamic metamaterial cloak for drag-free flow, Phys. Rev. Lett. 123 (2019): 074502, https://doi.org/10.1103/PhysRevLett.123.074502.

[12] M.Y. Chen, X.Y. Shen, Z. Chen, J.H.Y. Lo, Y. Liu, X.L. Xu, Y.L. Wu, L. Xu, Realizing the multifunctional metamaterial for fluid flow in a porous medium, Proc. Natl. Acad. Sci. U.S.A. 119 (2022): e2207630119, https://doi.org/10.1073/pnas.2207630119.

[13] Y. Xiao, Q.Y. Chen, Q. Hao, Inverse thermal design of nanoporous thin films for thermal cloaking, Mater. Today Phys. 21 (2021): 100477, https://doi.org/10.1016/j.mtphys.2021.100477.

[14] W. Sha, M. Xiao, M.Z. Huang, L. Gao, Topology-optimized freeform thermal metamaterials for omnidirectionally cloaking sensors, Mater. Today Phys. 28 (2022): 100880, https://doi.org/10.1016/j.mtphys.2022.100880.

[15] Y.F. Hua, C. Qian, H.S. Chen, H.P. Wang, Experimental topology-optimized cloak for water waves, Mater. Today Phys. 27 (2022): 100754, https://doi.org/10.1016/j.mtphys.2022.100754.

[16] C. Zhang, W.K. Cao, J. Yang, J.C. Ke, M.Z. Chen, L.T. Wu, Q. Cheng, T.J. Cui, Multiphysical digital coding metamaterials for independent control of broadband electromagnetic and acoustic waves with a large variety of functions, ACS Appl. Mater. Interfaces 11 (2019) 17050–17055, https://doi.org/10.1021/acsami.9b02490.

[17] Y. Zhou, J. Chen, R. Chen, W.J. Chen, Z. Fan, Y.G. Ma, Ultrathin electromagnetic–acoustic amphibious stealth coats, Adv. Opt. Mater. 8 (2020): 2000200, https://doi.org/10.1002/adom.202000200.

[18] Y. Li, K.J. Zhu, Y.G. Peng, W. Li, T.Z. Yang, H.X. Xu, H. Chen, X.F. Zhu, S.H. Fan, C. W. Qiu, Thermal meta-device in analogue of zero-index photonics, Nat. Mater. 18 (2019) 48–54, https://doi.org/10.1038/s41563-018-0239-6.

[19] L.J. Xu, G.L. Dai, J.P. Huang, Transformation multithermotics: controlling radiation and conduction simultaneously, Phys. Rev. Appl. 13 (2020): 024063, https://doi.org/10.1103/PhysRevApplied.13.024063.

[20] J.X. Li, Y. Li, P.C. Cao, T.Z. Yang, X.F. Zhu, W.Y. Wang, C.W. Qiu, A continuously tunable solid-like convective thermal metadevice on the reciprocal line, Adv. Mater. 32 (2020): 2003823, https://doi.org/10.1002/adma.202003823.

[21] L.J. Xu, J. Wang, G.L. Dai, S. Yang, F.B. Yang, G. Wang, J.P. Huang, Geometric phase, effective conductivity enhancement, and invisibility cloak in thermal convection-conduction, Int. J. Heat Mass Tran. 165 (2021): 120659, https://doi.org/10.1016/j.ijheatmasstransfer.2020.120659.

[22] J.Y. Li, Y. Gao, J.P. Huang, A bifunctional cloak using transformation media, J. Appl. Phys. 108 (2010): 074504, https://doi.org/10.1063/1.3490226.

[23] Y.G. Ma, Y.C. Liu, M. Raza, Y.D. Wang, S.L. He, Experimental demonstration of a multiphysics cloak: manipulating heat flux and electric current simultaneously, Phys. Rev. Lett. 113 (2014): 205501, https://doi.org/10.1103/PhysRevLett.113.205501.

[24] M. Moccia, G. Castaldi, S. Savo, Y. Sato, V. Galdi, Independent manipulation of heat and electrical current via bifunctional metamaterials, Phys. Rev. X 4 (2014): 021025, https://doi.org/10.1103/PhysRevX.4.021025.

[25] T.Z. Yang, X. Bai, D.L. Gao, L.Z.W.B.W. Li, J.T.L. Thong, C.W. Qiu, Invisible sensors: simultaneous sensing and camouflaging in multiphysical fields, Adv. Mater. 27 (2015) 7752–7758, https://doi.org/10.1002/adma.201502513.

[26] C.W. Lan, B. Li, J. Zhou, Simultaneously concentrated electric and thermal fields using fan-shaped structure, Opt Express 23 (2015) 24475–24483, https://doi.org/10.1364/OE.23.024475.

[27] T. Stedman, L.M. Woods, Cloaking of thermoelectric transport, Sci. Rep. 7 (2017) 6988, https://doi.org/10.1038/s41598-017-05593-6.

[28] S.X. Yin, E. Galiffi, A. Alù, Floquet metamaterials, eLight 2 (2022) 8, https://doi.org/10.1186/s43593-022-00015-1.

[29] E. Galiffi, R. Tirole, S.X. Yin, H.N. Li, S. Vezzoli, P.A. Huidobro, M.G. Silveirinha, R. Sapienza, A. Alù, J.B. Pendry, Photonics of time-varying media, Adv. Photonics 4 (2022): 014002, https://doi.org/10.1117/1.AP.4.1.014002.

[30] L. Zhang, X.Q. Chen, R.W. Shao, J.Y. Dai, Q. Cheng, G. Castaldi, V. Galdi, T.J. Cui, Breaking reciprocity with space-time-coding digital metasurfaces, Adv. Mater. 31 (2019): 1904069, https://doi.org/10.1002/adma.201904069.

[31] S. Taravati, G.V. Eleftheriades, Microwave space-time-modulated metasurfaces, ACS Photonics 9 (2022) 305–318, https://doi.org/10.1021/acsphotonics.1c01041.

[32] Z.X. Chen, Y.G. Peng, H.X. Li, J.J. Liu, Y.J. Ding, B. Liang, X.F. Zhu, Y.Q. Lu, J.C. Cheng, A. Alù, Efficient nonreciprocal mode transitions in spatiotemporally modulated acoustic metamaterials, Sci. Adv. 7 (2021): eabj1198, https://doi.org/10.1126/sciadv.abj1198.

[33] Y.R. Jia, Y.M. Liu, B.L. Hu, W. Xiong, Y.C. Bai, Y. Cheng, D. Wu, X.J. Liu, J. Christensen, Orbital angular momentum multiplexing in space–time thermoacoustic metasurfaces, Adv. Mater. 34 (2022) 2202026, https://doi.org/10.1002/adma.202202026.

[34] L.J. Xu, G.Q. Xu, J.P. Huang, C.W. Qiu, Diffusive fzeau drag in spatiotemporal thermal metamaterials, Phys. Rev. Lett. 128 (2022): 145901, https://doi.org/10.1103/PhysRevLett.128.145901.

[35] L.J. Xu, G.Q. Xu, J.X. Li, Y. Li, J.P. Huang, C.W. Qiu, Thermal willis coupling in spatiotemporal diffusive metamaterials, Phys. Rev. Lett. 129 (2022): 155901, https://doi.org/10.1103/PhysRevLett.129.155901.

[36] W.X. Zhao, Z. Zhu, Y.W. Fan, W. Xi, R. Hu, X.B. Luo, Temporally-adjustable radiative thermal diode based on metal-insulator phase change, Int. J. Heat Mass Tran. 185 (2022): 122443, https://doi.org/10.1016/j.ijheatmasstransfer.2021.122443.

[37] H.T. Wu, X.X. Gao, S. Liu, Q. Ma, H.C. Zhang, X. Wan, T.J. Cui, Robust Spin-momentum coupling induced by parity-time symmetric spatiotemporal metasurface, Adv. Opt. Mater. 9 (2021): 210132, https://doi.org/10.1002/adom.202101322.

[38] W.W. Zhu, H.R. Xue, J.B. Gong, Y.D. Chong, B.L. Zhang, Time-periodic corner states from Floquet higher-order topology, Nat. Commun. 13 (2022) 11, https://doi.org/10.1038/s41467-021-27552-6.

[39] G.Q. Xu, Y.H. Yang, X. Zhou, H.S. Chen, A. Alù, C.W. Qiu, Diffusive topological transport in spatiotemporal thermal lattices, Nat. Phys. 18 (2022) 450–456, https://doi.org/10.1038/s41567-021-01493-9.

[40] Z.J. Coppens, J.G. Valentine, Spatial and temporal modulation of thermal emission, Adv. Mater. 29 (2017): 1701275, https://doi.org/10.1002/adma.201701275.

[41] L. Zhang, X.Q. Chen, S. Liu, Q. Zhang, J. Zhao, J.Y. Dai, G.D. Bai, X. Wan, Q. Cheng, G. Castaldi, V. Galdi, T.J. Cui, Space-time-coding digital metasurfaces, Nat. Commun. 9 (2018) 4334, https://doi.org/10.1038/s41467-018-06802-0.

[42] L.L. Li, H.X. Ruan, C. Liu, Y. Li, Y. Shuang, A. Alù, C.W. Qiu, T.J. Cui, Machine-learning reprogrammable metasurface imager, Nat. Commun. 10 (2019) 1082, https://doi.org/10.1038/s41467-019-09103-2.

[43] J.B. Keller, A theorem on the conductivity of a composite medium, Physics 5 (1964) 548, https://doi.org/10.1063/1.1704146.

[44] K.S. Mendelson, A theorem on the effective conductivity of a two-dimensional heterogeneous medium, J. Appl. Phys. 46 (1975) 4740, https://doi.org/10.1063/1.321549.

[45] J. Nevard, J.B. Keller, Reciprocal relations for effective conductivities of anisotropic media, J. Math. Phys. 26 (1985) 2761–2765, https://doi.org/10.1063/1.526697.

[46] K. Schulgasser, A reciprocal theorem in two-dimensional heat transfer and its implications, Int. J. Heat Mass Tran. 19 (1992) 639, https://doi.org/10.1016/0735-1933(92)90047-L.

[47] S. Guenneau, C. Amra, D. Veynante, Transformation thermodynamics: cloaking and concentrating heat flux, Opt Express 20 (2012) 8207, https://doi.org/10.1364/OE.20.008207.

[48] S. Narayana, Y. Sato, Heat Flux Manipulation with engineered thermal materials, Phys. Rev. Lett. 108 (2012): 214303, https://doi.org/10.1103/PhysRevLett.108.214303.

[49] T. Han, T. Yuan, B. Li, C.W. Qiu, Homogeneous thermal cloak with constant conductivity and tunable heat localization, Sci. Rep. 3 (2013) 1593, https://doi.org/10.1038/srep01593.

[50] J.X. Li, Y. Li, T. Li, T.L. Li, W.Y. Wang, L.Q. Li, C.W. Qiu, Doublet thermal metadevice, Phys. Rev. Appl. 11 (2019): 044021, https://doi.org/10.1103/PhysRevApplied.11.044021.